

Measurement of the J/ψ photoproduction cross section over the full near-threshold kinematic region

S. Adhikari,²⁶ F. Afzal,³ C. S. Akondi,⁹ M. Albrecht,²⁹ M. Amarian,²⁶ V. Arroyave,⁸ A. Asaturyan,^{25,36} A. Austregesilo,²⁹ Z. Baldwin,⁴ F. Barbosa,²⁹ J. Barlow,⁹ E. Barriga,⁹ R. Barsotti,¹⁴ T. D. Beattie,²⁷ V. V. Berdnikov,⁵ T. Black,²⁵ W. Boeglin,⁸ W. J. Briscoe,¹⁰ T. Britton,²⁹ W. K. Brooks,²⁸ D. Byer,⁷ E. Chudakov,²⁹ P. L. Cole,¹⁷ O. Cortes,¹⁰ V. Crede,⁹ M. M. Dalton,²⁹ D. Darulis,¹¹ A. Deur,²⁹ S. Dobbs,⁹ A. Dolgolenko,¹⁶ R. Dotel,⁸ M. Dugger,¹ R. Dzhygadlo,¹² D. Ebersole,⁹ H. Egiyan,²⁹ T. Erborá,⁸ P. Eugenio,⁹ A. Fabrizi,¹⁹ C. Fanelli,³⁴ S. Fang,¹³ S. Fegan,¹⁰ J. Fitches,¹¹ A. M. Foda,¹² S. Furlotov,²⁹ L. Gan,²⁵ H. Gao,⁷ A. Gardner,¹ A. Gasparian,²⁴ C. Gleason,^{14,32} K. Goetzen,¹² V. S. Goryachev,¹⁶ B. Grube,²⁹ J. Guo,⁴ L. Guo,⁸ T. J. Hague,²⁴ H. Hakobyan,²⁸ J. Hernandez,⁹ N. D. Hoffman,⁴ D. Hornidge,²² G. Hou,¹³ G. M. Huber,²⁷ P. Hurck,¹¹ A. Hurley,³⁴ W. Imoehl,⁴ D. G. Ireland,¹¹ M. M. Ito,⁹ I. Jaegle,²⁹ N. S. Jarvis,⁴ T. Jeske,²⁹ R. T. Jones,⁶ V. Kakoyan,³⁶ G. Kalicy,⁵ V. Khachatryan,¹⁴ M. Khachatryan,⁸ C. Kourkoumelis,² A. LaDuke,⁴ I. Larin,^{19,16} D. Lawrence,²⁹ D. I. Lersch,²⁹ H. Li,⁴ W. B. Li,³⁴ B. Liu,¹³ K. Livingston,¹¹ G. J. Lolos,²⁷ L. Lorenti,³⁴ V. Lyubovitskij,^{31,30} D. Mack,²⁹ A. Mahmood,²⁷ P. P. Martel,^{22,18} H. Marukyan,³⁶ V. Matveev,¹⁶ M. McCaughan,²⁹ M. McCracken,^{4,33} C. A. Meyer,⁴ R. Miskimen,¹⁹ R. E. Mitchell,¹⁴ K. Mizutani,²⁹ V. Neelamana,²⁷ L. Ng,⁹ E. Nissen,²⁹ S. Orešić,²⁷ A. I. Ostrovidov,⁹ Z. Papandreou,²⁷ C. Paudel,⁸ R. Pedroni,²⁴ L. Pentchev,^{29,*} K. J. Peters,¹² E. Prather,⁶ S. Rakshit,⁹ J. Reinhold,⁸ A. Remington,⁹ B. G. Ritchie,¹ J. Ritman,^{12,15} G. Rodriguez,⁹ D. Romanov,²¹ K. Saldana,¹⁴ C. Salgado,²³ S. Schadmand,¹² A. M. Schertz,¹⁴ K. Scheuer,³⁴ A. Schick,¹⁹ A. Schmidt,¹⁰ R. A. Schumacher,⁴ J. Schwiening,¹² P. Sharp,¹⁰ X. Shen,¹³ M. R. Shepherd,¹⁴ A. Smith,⁷ E. S. Smith,³⁴ D. I. Sober,⁵ S. Somov,²¹ A. Somov,²⁹ J. R. Stevens,³⁴ I. I. Strakovsky,¹⁰ B. Sumner,¹ K. Suresh,²⁷ V. V. Tarasov,¹⁶ S. Taylor,²⁹ A. Teymurazyan,²⁷ A. Thiel,³ T. Viducic,²⁶ T. Whitlatch,²⁹ N. Wickramaarachchi,⁵ M. Williams,²⁰ Y. Wunderlich,³ B. Yu,⁷ J. Zarling,²⁷ Z. Zhang,³⁵ Z. Zhao,⁷ X. Zhou,³⁵ J. Zhou,⁷ and B. Zihlmann²⁹

(GLUEX Collaboration)

¹Arizona State University, Tempe, Arizona 85287, USA²National and Kapodistrian University of Athens, 15771 Athens, Greece³Helmholtz-Institut für Strahlen- und Kernphysik Universität Bonn, D-53115 Bonn, Germany⁴Carnegie Mellon University, Pittsburgh, Pennsylvania 15213, USA⁵The Catholic University of America, Washington, D.C. 20064, USA⁶University of Connecticut, Storrs, Connecticut 06269, USA⁷Duke University, Durham, North Carolina 27708, USA⁸Florida International University, Miami, Florida 33199, USA⁹Florida State University, Tallahassee, Florida 32306, USA¹⁰The George Washington University, Washington, D.C. 20052, USA¹¹University of Glasgow, Glasgow G12 8QQ, United Kingdom¹²GSI Helmholtzzentrum für Schwerionenforschung GmbH, D-64291 Darmstadt, Germany¹³Institute of High Energy Physics, Beijing 100049, People's Republic of China¹⁴Indiana University, Bloomington, Indiana 47405, USA¹⁵IKP, Forschungszentrum Jülich, D-52428 Jülich GmbH, Germany¹⁶National Research Centre Kurchatov Institute, Moscow 123182, Russia¹⁷Lamar University, Beaumont, Texas 77710, USA¹⁸Johannes Gutenberg-Universität Mainz, 55128 Mainz, Germany¹⁹University of Massachusetts, Amherst, Massachusetts 01003, USA²⁰Massachusetts Institute of Technology, Cambridge, Massachusetts 02139, USA²¹National Research Nuclear University Moscow Engineering Physics Institute, Moscow 115409, Russia²²Mount Allison University, Sackville, New Brunswick E4L 1E6, Canada²³Norfolk State University, Norfolk, Virginia 23504, USA²⁴North Carolina A&T State University, Greensboro, North Carolina 27411, USA²⁵University of North Carolina at Wilmington, Wilmington, North Carolina 28403, USA²⁶Old Dominion University, Norfolk, Virginia 23529, USA²⁷University of Regina, Regina, Saskatchewan S4S 0A2, Canada²⁸Universidad Técnica Federico Santa María, Casilla 110-V Valparaíso, Chile²⁹Thomas Jefferson National Accelerator Facility, Newport News, Virginia 23606, USA³⁰Tomsk Polytechnic University, 634050 Tomsk, Russia

*pentchev@jlab.org

³¹*Tomsk State University, 634050 Tomsk, Russia*³²*Union College, Schenectady, New York 12308, USA*³³*Washington & Jefferson College, Washington, Pennsylvania 15301, USA*³⁴*William & Mary, Williamsburg, Virginia 23185, USA*³⁵*Wuhan University, Wuhan, Hubei 430072, People's Republic of China*³⁶*A. I. Alikhanian National Science Laboratory (Yerevan Physics Institute), 0036 Yerevan, Armenia*

(Received 26 April 2023; accepted 15 June 2023; published 3 August 2023)

We report the total and differential cross sections for J/ψ photoproduction with the large acceptance GlueX spectrometer for photon beam energies from the threshold at 8.2 GeV up to 11.44 GeV and over the full kinematic range of momentum transfer squared, t . Such coverage facilitates the extrapolation of the differential cross sections to the forward ($t = 0$) point beyond the physical region. The forward cross section is used by many theoretical models and plays an important role in understanding J/ψ photoproduction and its relation to the J/ψ -proton interaction. These measurements of J/ψ photoproduction near threshold are also crucial inputs to theoretical models that are used to study important aspects of the gluon structure of the proton, such as the gluon generalized parton distribution of the proton, the mass radius of the proton, and the trace anomaly contribution to the proton mass. We observe possible structures in the total cross section energy dependence and find evidence for contributions beyond gluon exchange in the differential cross section close to threshold, both of which are consistent with contributions from open-charm intermediate states.

DOI: [10.1103/PhysRevC.108.025201](https://doi.org/10.1103/PhysRevC.108.025201)

I. INTRODUCTION

Over the past several years there has been a renewed interest in studying near-threshold J/ψ photoproduction as a tool to experimentally probe important properties of the nucleon related to its gluon content. Such experiments became possible thanks to the 12 GeV upgrade of the CEBAF accelerator at Jefferson Lab covering the threshold region of the reaction, resulting in the first exclusive measurements very close to threshold by the GlueX collaboration [1].

Exclusive J/ψ photoproduction is expected to proceed dominantly through gluon exchange due to the heavy mass of the charm quark. Thus, the t dependence of the reaction is defined by the proton vertex, which provides a probe of the nucleon gluon form factors [2]. The extraction of the gluonic properties of the proton from J/ψ production data requires additional assumptions. One such assumption is the use of vector meson dominance (VMD) to relate the $\gamma p \rightarrow J/\psi p$ reaction to elastic $J/\psi p \rightarrow J/\psi p$ scattering. At low energies, the latter reaction is related to several fundamental quantities. These include the trace anomaly contribution to the mass of the proton [3–5], and the $J/\psi p$ scattering length which is related to the possible existence of a charmonium-nucleon bound state [6,7].

An important QCD approach is to assume factorization between the gluon generalized parton distributions (gGPD) of the proton and the J/ψ wave function, and the hard quark-gluon interaction. The hard scale in this approach is defined by the heavy quark mass. In Ref. [8] such a general approach was applied to the J/ψ photoproduction in leading-order (LO) and next-to-leading-order (NLO) at high energy and small transferred momentum $|t|$. An important continuation of these efforts can be found in Refs. [9,10], where it was shown in LO and for heavy quark masses, that factorization also holds at energies down to threshold for large absolute values of

t . Close to threshold, due to the large skewness parameter, the spin-2 (graviton-like) two-gluon exchange dominates [9] and therefore J/ψ photoproduction can be used to study the gravitational form factors of the proton [10]. Such information was used to estimate the *mass* radius of the proton [11–14], as opposed to the well-known *charge* radius. Alternatively, the holographic approach was used to describe the soft part of J/ψ photoproduction and relate the differential cross sections to the gravitational form factors [4,13,15–17].

However, such an ambitious program to study the mass properties of the proton requires detailed investigation of the above assumptions used to interpret the data. Reference [18] calculates directly Feynman diagrams of the near-threshold heavy quarkonium photoproduction at large momentum transfer and finds that there is no direct connection to the gravitational form factors. In contrast to the above gluon-exchange mechanisms, it was proposed in Ref. [19] that J/ψ exclusive photoproduction may proceed through open-charm exchange, namely $\Lambda_c \bar{D}^{(*)}$. The authors point out that the thresholds for these intermediate states are very close to the J/ψ threshold and their exchange can contribute to the reaction. They predict cusps in the total cross section at the $\Lambda_c \bar{D}$ and $\Lambda_c \bar{D}^*$ thresholds. If such a mechanism would dominate over the gluon-exchange mechanism, then it would obscure the relation between J/ψ exclusive photoproduction and the gluonic properties of the proton together with all the important physical implications discussed above.

Furthermore, understanding the contribution of any processes besides gluon exchange to J/ψ photoproduction is crucial for the search for the photoproduction of the LHCb P_c^+ pentaquark candidates [20,21]. The P_c^+ states can be produced in the s -channel of the $\gamma p \rightarrow J/\psi p$ reaction, and the strength of this resonant contribution can be related to the branching fraction of $P_c^+ \rightarrow J/\psi p$ under the assumptions of VMD and a dominant nonresonant gluon exchange [22–25].

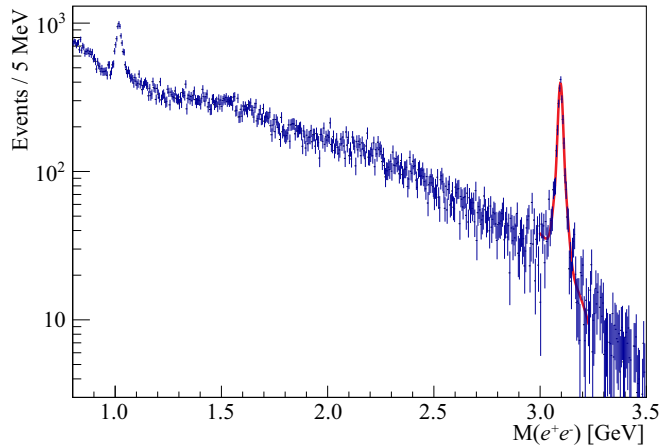


FIG. 1. The e^+e^- invariant mass spectrum for the GlueX phase I data set after applying the selections described in Sec. III. The J/ψ peak is fitted with a linear function and two Gaussians with common mean, which yields a total of $2270 \pm 58 J/\psi$'s.

If there would be significant contributions from other processes, such as the open-charm exchange mentioned above, then both of these assumptions break down. Therefore, a better understanding of all the processes that contribute to J/ψ photoproduction is required before updated searches for the P_c^+ can be performed.

In this work we report on the measurement of J/ψ exclusive photoproduction,

$$\gamma p \rightarrow J/\psi p \rightarrow e^+e^- p, \quad (1)$$

based on the data collected by phase I of the GlueX experiment [26] during the period 2016–2018. This data sample is more than four times larger than the one used in the first GlueX publication [1]. We present results for the total cross section for photon beam energies from threshold, $E_\gamma = 8.2$, up to 11.4 GeV. We also present the differential cross sections, $d\sigma/dt$, in three regions of photon beam energy over the full kinematic space in momentum transfer t , from $|t|_{\min}(E_\gamma)$ to $|t|_{\max}(E_\gamma)$, thanks to the full acceptance of the GlueX detector for this reaction. We identify the J/ψ particle through its decay into an electron-positron pair. Due to the wide acceptance for the exclusive reaction $\gamma p \rightarrow e^+e^- p$, we observe events in a broad range of e^+e^- invariant masses, including peaks corresponding to the ϕ and J/ψ mesons and the continuum between the two peaks that is dominated by the nonresonant Bethe-Heitler (BH) process (see Fig. 1). As an electromagnetic process that is calculable to a high accuracy, we will use the measurement of this BH process for the absolute normalization of the J/ψ photoproduction cross sections.

II. THE GLUEX DETECTOR

The experimental setup is described in detail in Ref. [26]. The GlueX experiment uses a tagged photon beam, produced on a diamond radiator from coherent Bremsstrahlung of the initial electron beam from the CEBAF accelerator. The scattered electrons are deflected by a 9 T m dipole magnet and detected in a tagging array which consists of scintillator

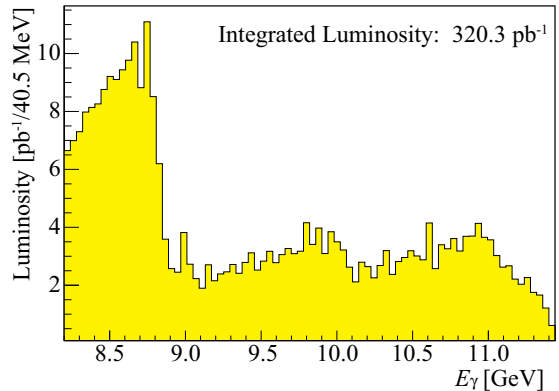


FIG. 2. The measured tagged photon spectrum for GlueX phase I in units of luminosity. The nonstatistical fluctuations are due to the segmentation of the tagger.

paddles and fibers, that allows determination of the photon energy with 0.2% resolution. The photons are collimated by a 5-mm-diameter hole placed at 75 m downstream of the radiator. The flux of the photon beam is measured with a pair spectrometer (PS) [27] downstream of the collimator, which detects electron-positron pairs produced in a thin converter. For most of phase I, the electron beam energy was 11.7 GeV, corresponding to about 11.4 GeV maximum tagged photon energy. The coherent peak was kept in the region of 8.2–9.0 GeV, which is just above the J/ψ threshold; see Fig. 2. The produced photon beam is substantially linearly polarized in this peak region and the orientation of the polarization was changed periodically, although the beam polarization was not used in this analysis. The bunches (≈ 1 ps long) in the electron and secondary photon beams are 4 ns apart for almost all of the data.

The GlueX detector is built around a 2 T solenoid, which is 4 m long and has an inner diameter of the bore of 1.85 m. A liquid Hydrogen target that is 30 cm long, is placed inside the magnet. It is surrounded by a start counter [28], a segmented scintillating detector with a timing resolution of 250 to 300 ps, that helps us to choose the correct beam bunch. The tracks of the final state charged particles are reconstructed using two drift chamber systems. The central drift chamber (CDC) [29] surrounds the target and consists of 28 layers of straw tubes (about 3500 in total) with axial and stereo orientations. The low amount of material in the CDC allows tracking of the recoil protons down to momenta p_p as low as 0.25 GeV and identify them via the energy losses for $p_p < 1$ GeV. In the forward direction, but still inside the solenoid, the forward drift chamber (FDC) [30] system is used to track charged particles. It consists of 24 planes of drift chambers grouped in four packages with both wire and cathode-strip (on both sides of the wire plane) readouts, in total more than 14 000 channels. Such geometry allows reconstruction of space points in each plane and separation of trajectories in the case of high particle fluxes present in the forward direction.

Electrons and positrons are identified by two electromagnetic calorimeters. The barrel calorimeter (BCAL) [31] is inside the magnet and surrounds the two drift chamber

systems. It consists of lead layers and scintillating fibers, grouped in 192 azimuthal segments and four radial layers, allowing reconstruction of the longitudinal and transverse shower development. The forward calorimeter (FCAL) covers the downstream side of the acceptance outside of the magnet at about 6 m from the target and consists of 2800 lead-glass blocks of $(4 \times 4 \times 45) \text{ cm}^3$. A Time-of-Flight scintillator wall is placed just upstream of the FCAL.

The two calorimeters, BCAL and FCAL, are used to trigger the detector readout with a requirement of sufficient total energy deposition. The trigger threshold is optimized for the collection of minimum ionizing events and is much lower than the sum of the energy of the two leptons for the reactions discussed in this paper. The intensity of the beam in the energy region above the J/ψ threshold gradually increased from about 2×10^7 photons/s in 2016 to about 10^8 photons/s at the end of 2018, resulting in a total integrated luminosity of 320 pb^{-1} .

III. DATA ANALYSIS

A key feature of our measurement is that the GlueX detector has essentially full acceptance for the J/ψ photoproduction in Eq. (1). For photoproduction of light mesons, the acceptance of the recoil proton is limited at low momentum where the protons do not reach the drift chambers. However, due to the high mass of the J/ψ meson, the recoil proton has a minimum momentum of 0.6 GeV and can be reliably detected. Geometrically, the GlueX detector has full azimuthal acceptance and 1° – 120° polar angle coverage, allowing detection of all the final state particles in the whole kinematic region of the reaction. Thus, the total cross section of the exclusive reaction is measured directly, without any assumptions about the final state particles or extrapolations to kinematic regions outside of the acceptance.

The three final state particles are required to originate within the time of the same beam bunch. The beam photons whose time (as determined by the tagger) coincide with this bunch are called in-time photons and they qualify as candidates associated with this event. The other, out-of-time, tagged photons are used to estimate the fraction of events that are “accidentally” associated with an in-time photon that did not produce the reconstructed final state particles. Unless otherwise noted, all the distributions shown in this paper have the corresponding accidental background contributions subtracted.

The exclusivity of the measurement, together with the precise knowledge of the beam energy and its direction, allows performing of a kinematic fit. The fit requires four-momentum conservation and a common vertex of the final state particles. A very loose selection criterion is applied to the χ^2 value of the fit. The momentum of the recoil proton, p_p is relatively well measured, as the protons are produced at moderate polar angles ($\theta \approx 10$ – 30°) with $p_p \approx 1 \text{ GeV}$. This is not the case for the lepton pair, where one of the leptons is predominantly produced with a high momentum at a small polar angle, i.e., in a region with a poor momentum resolution of the solenoidal spectrometer. The kinematic fit to the full reaction is therefore constrained mainly by the direction and magnitude of the

proton momentum and the direction of the lepton momenta, which are measured more precisely than the magnitudes of the lepton momenta. After applying the kinematic fit, the J/ψ mass resolution improves significantly to about 13 MeV (see Fig. 1).

Monte Carlo simulations for both J/ψ and BH processes have been performed. To calculate the absolute BH cross section, we have used a generator [32] based on analytic calculations of the BH cross sections [33]. For the proton form factors that enter in the calculations, we use the low- Q^2 parametrization of Ref. [34]. We note that if the dipole form factors are used instead, the BH cross section differs by less than 1% within the kinematic region used for normalization. The J/ψ events were generated using a t dependence and an energy dependence of the cross section obtained from smooth fits to our measurements. For the J/ψ decay, photon-to- J/ψ spin projection conservation in the Gottfried-Jackson frame is assumed. This corresponds to a $1 + \cos^2 \theta_{\text{GJ}}$ angular distribution of the decay particles, where θ_{GJ} is the lepton polar angle in the Gottfried-Jackson frame.

To simulate the detector response we have used the GEANT4 package [35]. In addition, to the generated events, we include accidental tagger signals and detector noise hits extracted from data collected with an asynchronous trigger. These simulations are used to calculate the reconstruction efficiencies for the two processes, ε_{BH} and $\varepsilon_{J/\psi}$. The BH simulations are also used to integrate the absolute cross sections in the kinematic regions used for normalization.

We use the BH process in the e^+e^- invariant mass region of $1.2 < M(e^+e^-) < 2.5 \text{ GeV}$ for the absolute normalization of the J/ψ total cross section, thus eliminating uncertainties from sources like luminosity and reconstruction efficiencies that are common for both processes. The main challenge in extracting the BH yields is to separate the pure e^+e^- continuum from the background of $\pi^+\pi^-$ production that is more than three orders of magnitude more abundant. We suppress the pions primarily using the energy deposition E in the calorimeters and requiring both lepton candidates to have p/E consistent with unity, where p is the momentum determined from the kinematic fit. In addition, we use the inner layer of the BCAL as a preshower detector and require the energy deposition there to be $E_{\text{pre}} \sin \theta > 30 \text{ MeV}$, where $\sin \theta$ corrects for the path length in the preshower layer. The pion background is further reduced by selecting the kinematic region with particle momenta $p > 0.4 \text{ GeV}$, to remove pions coming from target excitations. In addition, for the BH measurements only, we select $|t| < 0.6 \text{ GeV}^2$ as the BH cross section is dominated by the pion background above this t value, due to the very sharp t dependence of the BH process. After applying all of the selection criteria above, the remaining background is of approximately the same magnitude as the signal. The final BH yields are extracted by subtracting this pion background using the procedure described below.

We extract the yields of the leptons detected in the BCAL and FCAL separately, since the calorimeters have different resolutions. We perform this procedure in bins of the beam energy or other kinematic variables. For illustration only, in Figs. 3 and 4 we demonstrate this procedure over one energy bin ($8.92 < E_\gamma < 9.10 \text{ GeV}$), including leptons detected in

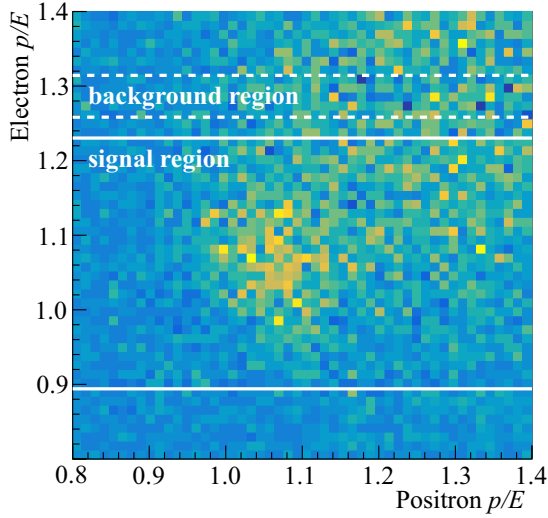


FIG. 3. Electron vs positron p/E distribution in the BH invariant mass region of 1.2–2.5 GeV. The white horizontal lines indicate the background and signal regions used when projecting onto the positron axis. See text for explanations.

both calorimeters. We consider the two-dimensional p/E distribution of electron versus positron candidates, and define a one-dimensional $\pm 3\sigma_{p/E}$ signal region around the p/E peak of one of the leptons. The projection of this region onto the p/E axis of the second lepton is shown in Fig. 4(a) (full black points). The shape of the pion background is estimated using events outside of the p/E peak of the first lepton (the background region indicated in Fig. 3), to which we fit a polynomial function of third order. The events in the signal region [full black points in Fig. 4(a)] are then fit with a sum of a Gaussian and this polynomial, where the latter is multiplied by a free normalization parameter, B_{norm} . The background distribution scaled by B_{norm} is shown by the open blue points in Fig. 4(a). The lepton yields are extracted by fitting the difference of the distribution in the signal region (full black points)

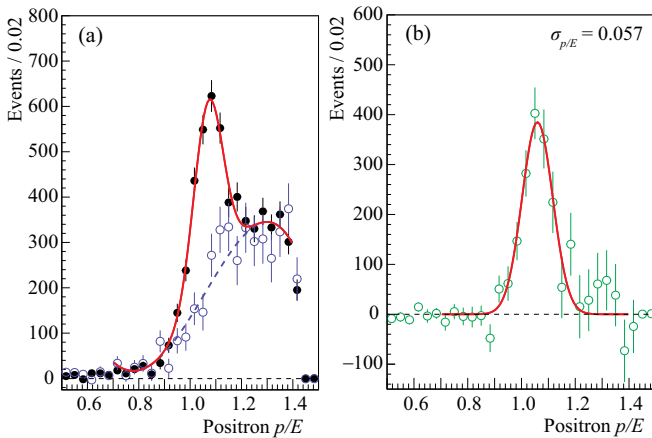


FIG. 4. (a) The p/E distributions in the signal (solid black) and background (open blue) region for the BH invariant mass region of 1.2–2.5 GeV. (b) The difference between the signal and background distributions from panel (a). See text for explanation of the fits.

and the scaled background distribution (open blue points) with a Gaussian, shown in Fig. 4(b). We perform this procedure for both positrons and electrons. For each species, the yields are extracted separately for the cases where the selected lepton is detected by the BCAL or the FCAL (regardless of where the other lepton is detected). We then average the summed yields for electrons and positrons to estimate the BH yields. To estimate the systematic uncertainty of this procedure at each data point, two variations of the method are tested. They differ by fixing the width of the p/E peak to the simulations (default for the central value) or leaving it as a free parameter. We also vary the method of integrating the signal, either by summing the histogram values in Fig. 4(b) (default) or integrating the fitted function. The results of these variations are discussed in Sec. IV.

As a check of the validity of our reconstruction procedure, we extract the BH cross section from our data and compare it to the expectations from the absolute calculations described previously. The fitting procedure described above is applied in bins of various kinematic quantities, e.g., E_γ , and we extract the cross section as

$$\sigma_{\text{BH}}^{\text{data}}(E_\gamma) = \frac{N_{\text{BH}}(E_\gamma)}{L(E_\gamma)\varepsilon_{\text{BH}}(E_\gamma)}, \quad (2)$$

where N_{BH} is the measured BH yield in a specific photon-energy bin, ε_{BH} is the corresponding reconstruction efficiency determined from MC simulations, and L is the measured luminosity. We note that the photon beam luminosity is used just for this study as a cross-check, but not for the final J/ψ cross sections that are determined relative to these BH cross sections.

The BH cross sections as function of the beam energy, extracted from Eq. (2), are compared with the MC calculations in Fig. 5. The data/MC ratio of the cross sections [Fig. 5(b)] is consistent with a constant and differs from unity by about 15%. Since this ratio is approximately constant over the kinematic region under consideration, we take its difference from unity as an estimation of the overall systematic uncertainty in the normalization of our cross sections. Similar ratios as a function of other kinematic variables, including proton momentum and polar angle, have been studied. Although the BH cross section varies by up to two orders of magnitude across these variables, the data and MC results remain consistent. In Fig. 6 we show one such comparison as a function of the invariant mass, $M(e^+e^-)$, which illustrates how well the BH simulations describe the data from the region used for normalization (1.2–2.5 GeV) to the J/ψ peak. We see a slight increase in the data/MC ratio in the region close to the J/ψ peak, which, however, is not statistically significant and is within the 15% uncertainty estimated above.

To measure the J/ψ yields, we apply the same event selections as for the BH process described above, except that we do not constrain the $|t|$ range. We select lepton candidates using $\pm 3\sigma_{p/E}$ selections, however, in contrast to the BH continuum, no additional p/E fitting procedure is needed to separate the pion background. Instead, we separate J/ψ candidates from the background by fitting the narrow J/ψ peak in the $M(e^+e^-)$ distributions. We fit the mass distributions in 18 bins of the beam energy with a Gaussian for the J/ψ

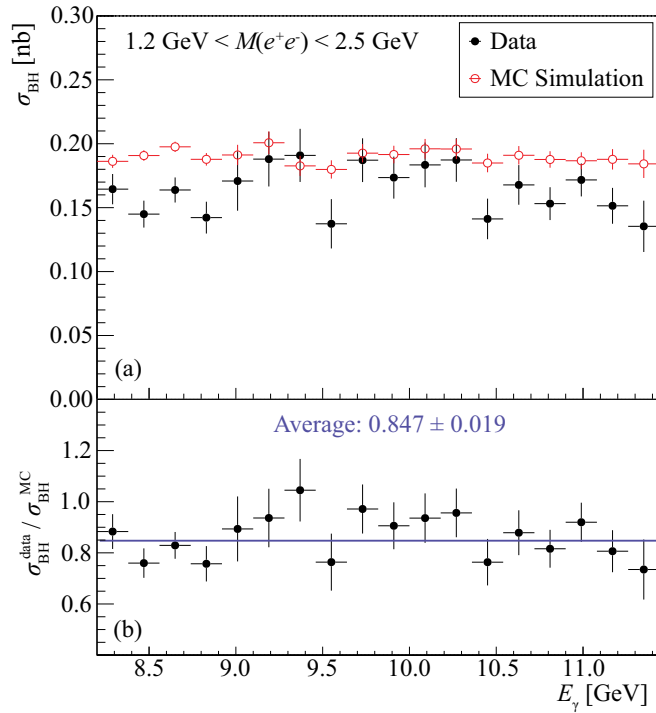


FIG. 5. BH cross section vs beam photon energy for $1.2 < M(e^+e^-) < 2.5 \text{ GeV}$. (a) BH cross section obtained from data and MC simulation. (b) Ratio of data and MC cross sections from panel (a) fitted with a constant.

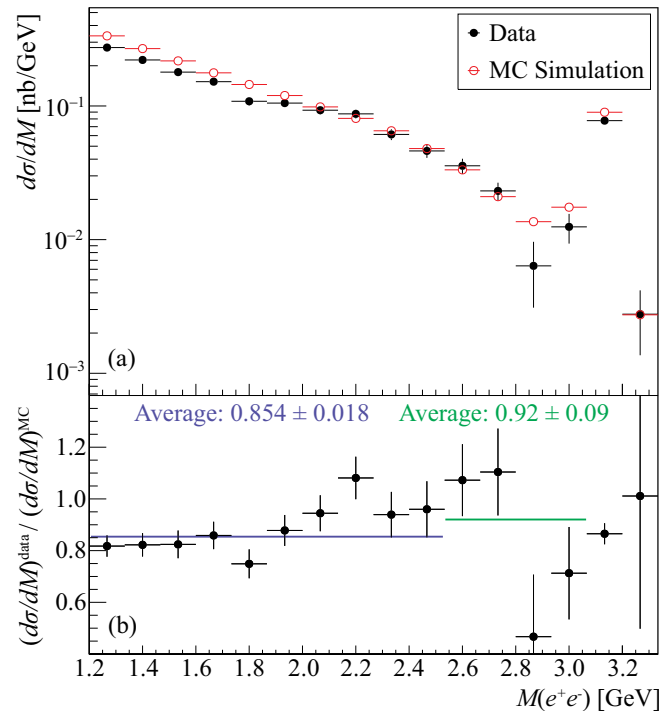


FIG. 6. The sum of BH and J/ψ cross sections as function of e^+e^- invariant mass. (a) Cross section obtained from data and MC simulation. (b) Ratio of data and MC cross sections from panel (a) fitted with constants in two regions: the region used for normalization of the J/ψ cross section, and the vicinity of the J/ψ peak.

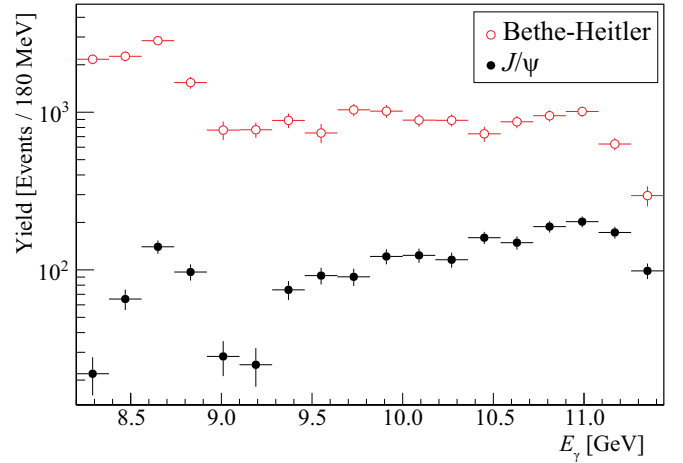


FIG. 7. Comparison of BH and J/ψ yields as function of beam energy.

peak plus a linear background. Because of the fine binning and the resulting small sample size in each bin, we employ the binned maximum-likelihood method, where Poisson errors are assumed in each invariant-mass bin, using the *RootFit* package [36]. Our studies show that the background due to accidental beam photon combinations in this mass region is small (about 5%) and of similar shape to the other smooth backgrounds, so in this case we do not explicitly subtract these accidental combinations. We perform fits, where we leave the Gaussian width of the J/ψ peak as a free parameter and where we fix it to the expectation from MC simulation. The fitted widths of the J/ψ peaks match well the expectations from simulation. We hence fix the widths to obtain our nominal results and use the results with free widths to estimate the systematic uncertainty in our knowledge of the peak shape. To study the systematic uncertainty of the lepton identification we also vary the p/E selections, and include these variations as described below.

IV. TOTAL CROSS SECTION

The extracted J/ψ and BH yields as a function of beam energy are compared in Fig. 7. While the BH yields follow the beam intensity spectrum, the J/ψ yields exhibit an indication of a dip in the 9.1 GeV region which will be discussed below. For illustration, individual J/ψ mass fits for four energy bins around 9.1 GeV are shown in Fig. 8. The beam photon flux varies strongly in this region, so to correct for this effect we scale the yield by the flux for the corresponding energy bin.

We calculate the total cross section as a function of beam energy using the following formula:

$$\sigma(E_\gamma) = \frac{N_{J/\psi}(E_\gamma)}{N_{\text{BH}}(E_\gamma)} \frac{\sigma_{\text{BH}}(E_\gamma)}{\text{BR}_{J/\psi}} \frac{\varepsilon_{\text{BH}}(E_\gamma)}{\varepsilon_{J/\psi}(E_\gamma)}. \quad (3)$$

Here $N_{J/\psi}$ and N_{BH} are the corresponding yields, σ_{BH} is the calculated BH cross section integrated over the region used for normalization, $\text{BR}_{J/\psi}$ is the $J/\psi \rightarrow e^+e^-$ branching ratio of 5.97% [37], and $\varepsilon_{J/\psi}$ and ε_{BH} are the MC-determined

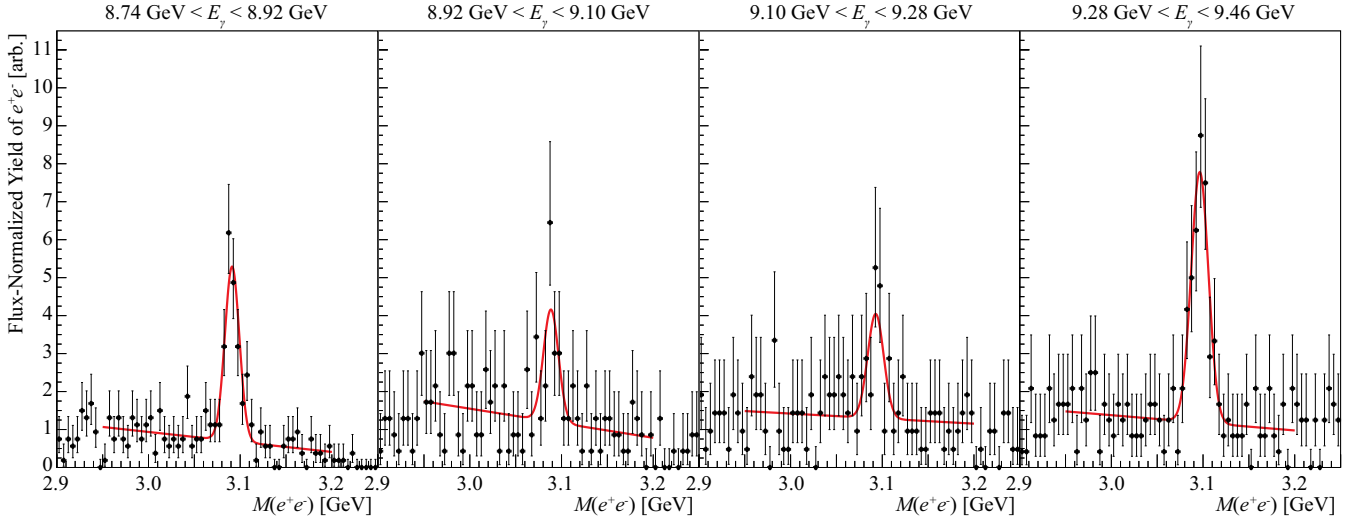


FIG. 8. Distribution of $M(e^+e^-)$ in bins of beam energy E_γ with fits to the J/ψ peak overlaid. The y axis of each histogram is scaled by the flux integrated over the corresponding E_γ bin.

efficiencies. Note that only the relative efficiency between the two processes enters in the above equation.

The calculations in Eq. (3) are shown in several steps in Fig. 9 to demonstrate that the possible dip structure at $E_\gamma \approx 9.1$ GeV arises from the yield ratio and not from the subsequent corrections. We note that the position of the dip coincides with a drop in the photon-beam intensity just above the coherent peak, as seen in Fig. 2; however, we performed studies showing that this is coincidental. In particular, as seen in Fig. 7, there is no dip in the BH yields in this region. Since the reconstruction of the e^+e^-p final state is strongly determined by the reconstruction of the recoil proton, we have also searched for a similar deviation in $p\bar{p}$ photoproduction,

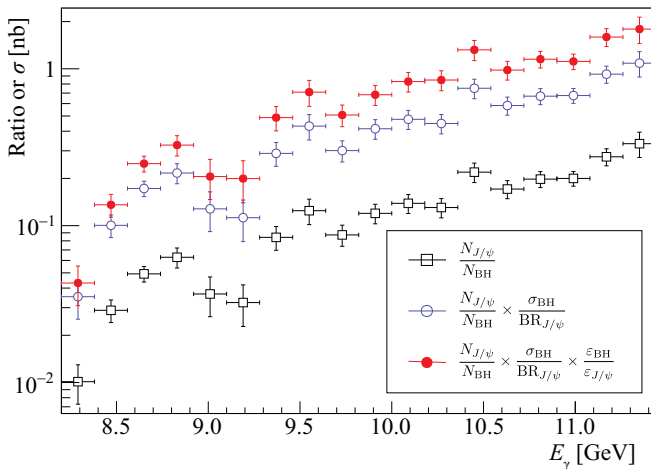


FIG. 9. Intermediate results of the J/ψ cross-section calculation: the J/ψ to BH yield ratio (black open squares); the yield ratio multiplied by the BH cross section over $BR(J/\psi \rightarrow e^+e^-)$ (blue open points); and this result further corrected by the BH-to- J/ψ efficiency ratio (solid red points) corresponding to the final cross section [see Eq. (3)]. The nb units are valid for the final result only (solid red points). Only the statistical errors are shown.

$\gamma p \rightarrow (p\bar{p})p$, where we require the $p\bar{p}$ invariant mass to be in the J/ψ mass region $3.05 < M(p\bar{p}) < 3.15$ GeV. With this selection, the recoil protons in this reaction are kinematically close to those in the $\gamma p \rightarrow J/\psi p$ reaction. We find that the flux normalized yields for the $p\bar{p}$ reaction as a function of photon energy are smooth in the region of the J/ψ dip.

The systematic uncertainties on the individual cross section points are taken from three sources as previously described. The systematic uncertainty in the BH yield extraction is determined by the maximum deviation in the two fitting variations from the nominal value, as discussed above. The systematic uncertainty in the J/ψ yield extraction is determined by taking the difference in the cross section values between the fits with fixed and free Gaussian widths. Additionally, we study the deviation in the cross section when widening the selected p/E region around the peak to $\pm 4\sigma$. To estimate this uncertainty, we use the photon flux instead of the BH cross section to calculate the cross section. This change in the normalization is required due to the difficulty of measuring the BH cross section with this looser E/p requirement. The uncertainties from each of the three contributions are added in quadrature to get the total systematic uncertainties. These values are illustrated in Fig. 10.

As mentioned above, we assume in the MC simulation a certain angular distribution of the J/ψ decay products, namely $1 + \cos^2 \theta_{GJ}$, where θ_{GJ} is the lepton polar angle in the Gottfried-Jackson frame, which corresponds to photon-to- J/ψ conservation of the spin projection in this frame. To estimate the systematic error related to this assumption, we compare the efficiency from this model to the extreme case when assuming uniform distribution. The variations of the efficiency as a function of energy do not exceed 5%. We also perform a fit to the measured θ_{GJ} distribution and find the results to be consistent with the assumption of spin projection conservation, which reduces the above upper limit on this uncertainty to a $< 2\%$ level. The measured total cross section is plotted in Fig. 11, with the statistical and total uncertainties shown separately. With the exception of the first point, the

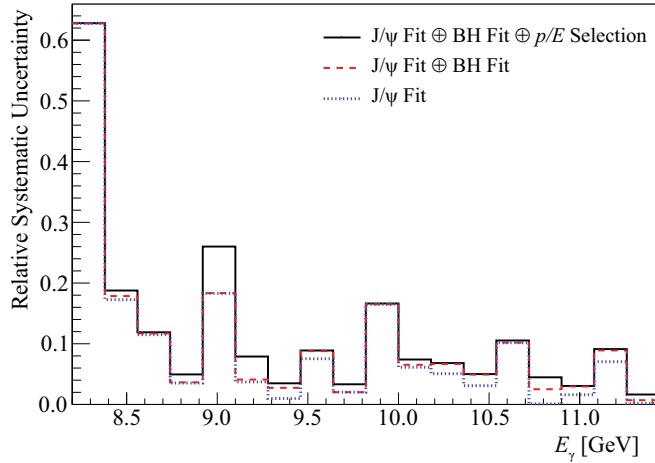


FIG. 10. Contributions of the different sources to the systematic uncertainties of the individual energy bins, successively added in quadrature.

statistical errors dominate. The numerical results for the total cross section, along with their statistical and systematic errors, are given in Table III of the Appendix.

The summary of the sources and magnitudes of the overall normalization uncertainties is given in Table I. The main source of this uncertainty was discussed in Sec. III, where we studied the BH data/MC ratio as a function of the beam energy and invariant mass. We use the $(15.3 \pm 1.9)\%$ average difference between data and MC, that is consistent with a constant function of energy (see Fig. 5), as a measure of the systematic uncertainty in the overall scale. The effect of the radiative corrections to the cross section was studied in the previous publication [1] based on Ref. [38]. The possible

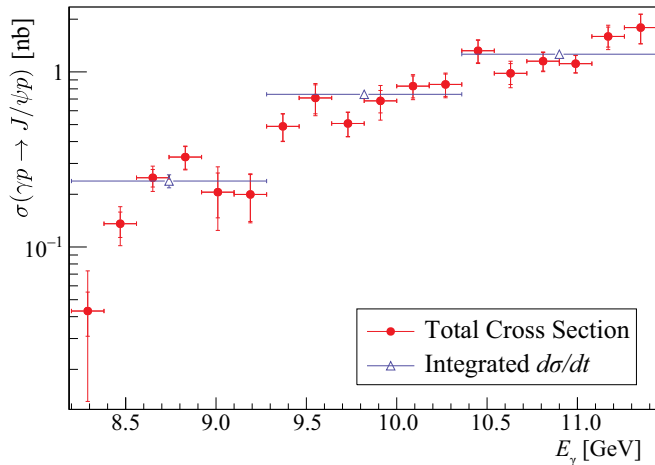


FIG. 11. The filled red points show the measured total cross sections obtained from Eq. (3) in fine photon energy bins. The inner bars represent the statistical errors and outer bars are the total errors, with the statistical and systematic errors added in quadrature. The open blue triangles represent the total cross sections calculated by integrating the functions fitted to the measured differential cross sections for the three beam energy regions, with only the statistical uncertainties shown.

TABLE I. Contributions to the overall normalization uncertainty and their sum in quadrature.

Source	Uncertainty
BH data-to-MC ratio vs E_γ	15.3%
Radiative corrections	8.3%
TCS contribution to BH	8%
ρ' contribution to BH	3.6%
Total	19.5%

contribution of the timelike Compton scattering (TCS) to the e^+e^- continuum was estimated in [1] using a generator [39] based on the calculations in Ref. [40]. To estimate the effect of a possible contribution of $\rho'(1600)$ to the $M(e^+e^-)$ region used for normalization, we fit the data/MC ratio versus invariant mass in Fig. 6 with constants in two regions, the standard one 1.2–2.5 GeV and the one over the $\rho'(1600)$ resonance region 1.46–1.86 GeV. The results are 0.854 ± 0.018 and 0.813 ± 0.031 , respectively. These results are consistent within the 3.6% combined error, which we conservatively take as a measure of this systematic uncertainty.

V. DIFFERENTIAL CROSS SECTIONS

We present measurements of the differential cross sections, $d\sigma/dt(E_\gamma, t)$, over the entire near-threshold kinematic region. The two-dimensional bins in the (E_γ, t) plane for which we report the cross section values are shown in Fig. 12. We subdivide the data into three equidistant energy ranges, while the t -bins match the crossing of these ranges with the $|t|_{\min}(E_\gamma)$ and $|t|_{\max}(E_\gamma)$ kinematic limits. Such a choice allows sufficient sample size in each bin. Because the variation of the beam-photon flux across each energy bin is rather large, we weight each event by the measured luminosity $L(E_\gamma)$ in steps of 45 MeV bins, i.e., the weight for E_γ bin i is

$$\text{weight}_i = \frac{1}{L(E_{\gamma i})[\text{nb}^{-1}]/0.045\text{GeV}}. \quad (4)$$

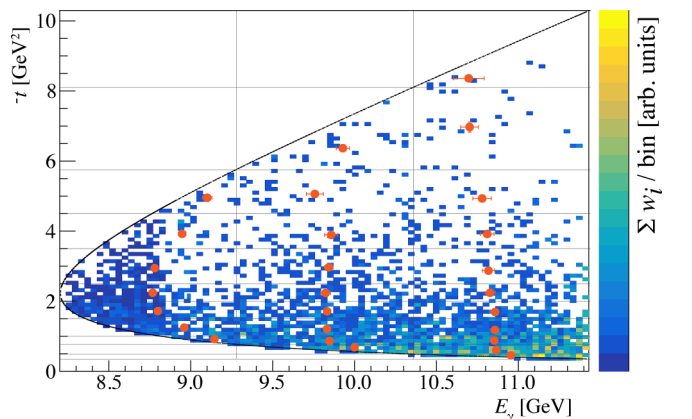


FIG. 12. The distribution of the flux-weighted data in the E_γ - t plane and the mean values of the reported cross sections (solid dots) within the corresponding bins. A mass selection of $3.05 < M(e^+e^-) < 3.15$ GeV is used for the events in this plot.

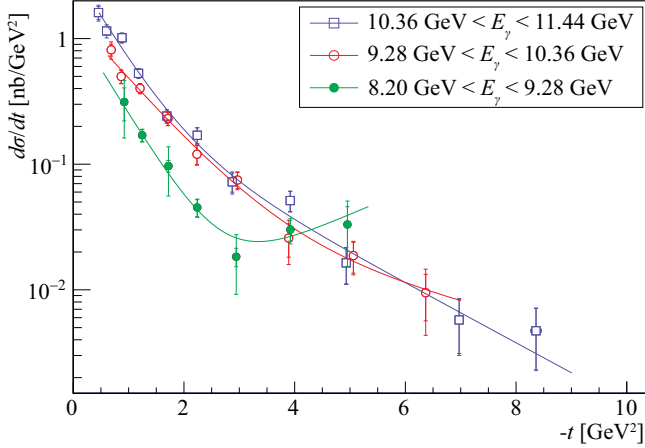


FIG. 13. The measured differential cross sections with both statistical (inner bars) and total (outer bars) uncertainties shown for the three energy regions, from Eq. (5). The points are fitted with a sum of two exponential functions. The second exponential contribution is most significant in the lowest energy bin, where the slope changes sign.

We then fit the weighted $M(e^+e^-)$ distribution to obtain a luminosity-weighted number of J/ψ events in each bin of E_γ and t , which we denote $N_{\text{wt}}^{J/\psi}(E_\gamma, t)$. The energy resolution as measured by the experimental setup is better than the 45 MeV bin size used in this procedure.

The cross sections are reported at the mean t and E_γ values within each bin (red points in Fig. 12). Note that for a given energy region, the mean E_γ values depend on the t bin. Still, we attribute a common mean energy within each energy region and treat the corresponding deviations of the cross section due to the energy correction as a systematic error. In addition, generally, the cross section averaged over the bin deviates from the cross section at the mean E_γ and t where it is reported, especially for the bins that are wide and have nonrectangular shapes. This deviation will also be treated as a systematic error.

To calculate the differential cross section, we divide the luminosity-weighted number of J/ψ events in each bin by the area of the bin, $a(E_\gamma, t)$, and correct for the reconstruction efficiency $\varepsilon(E_\gamma, t)$:

$$\frac{d\sigma}{dt}(E_\gamma, t) = \frac{N_{\text{wt}}^{J/\psi}(E_\gamma, t) [\text{GeV} \cdot \text{nb}]}{a(E_\gamma, t) [\text{GeV} \cdot \text{GeV}^2] \varepsilon(E_\gamma, t)}. \quad (5)$$

Thus, the differential cross section will be in units of $[\text{nb}/\text{GeV}^2]$. The area of each bin is calculated with MC by generating a uniform distribution over the whole rectangular (E_γ, t) plane in Fig. 12.

We apply the same procedure for the extraction of the J/ψ yields as explained in Sec. III for the total cross section. The efficiencies calculated from MC, $\varepsilon_{\text{MC}}(E_\gamma, t)$, are corrected by the overall normalization correction as obtained in Sec. III, using the BH process. Thus, in Eq. (5) we use $\varepsilon(E_\gamma, t) = \varepsilon_{\text{MC}}(E_\gamma, t) \times (0.847 \pm 0.019)$. Now we have all the ingredients in Eq. (5) to calculate the differential cross sections, and the results are given in Fig. 13. To parametrize

them, they are fitted with a sum of two exponential functions. To check the consistency of the differential cross sections, we integrate the fitted function over the corresponding range $t_{\text{min}}(E_{\gamma i}) - t_{\text{max}}(E_{\gamma i})$, where $E_{\gamma i}$ is the mean energy for the corresponding energy region, and compare these integrals with the total cross section results. We find a good agreement, shown in Fig. 11.

We consider three sources in the systematic uncertainties of the individual differential data points: (i) the uncertainty in the fitting procedure, (ii) the correction due to the alignment of the results to a common mean energy, and (iii) the bin-averaging effect. To estimate the last two effects, we create a two-dimensional cross section model based on our measurements. For that we use the fits of the differential cross sections in Fig. 13. The total cross section is also fitted with a polynomial. We note that these cross section parametrizations were used in the J/ψ generator for all the MC results presented in this paper. The main contribution to the systematic uncertainties for the individual data points comes from the J/ψ fitting procedure where we compare the yields extracted from a fit with either fixed widths (based on MC) or as a free parameter, in the same way as was done for the estimation of the systematic uncertainties in the total cross section.

The overall normalization uncertainty of the differential cross sections is the same as for the total cross section; see Table I.

The numerical results for the differential cross section, along with statistical and systematic errors, are given in Tables IV, V, and VI of the Appendix. Note that in all the plots in the next section, the error bars of the GlueX data points include both the statistical and systematic errors added in quadrature.

VI. DISCUSSION

In our cross section measurements, we observe two apparent deviations from the expectations: (i) of a smooth variation of the total cross section as a function of beam energy, and (ii) of an exponentially decreasing t dependence in the differential cross sections. We previously mentioned the structure in the 8.8–9.4 GeV region (Fig. 11) in Sec. IV. If we treat the two points there as a potential dip, then the probability that they are not a statistical fluctuation from a smooth fit to the observed cross sections corresponds to a significance of 2.6σ . However, if we consider the probability for any two adjacent points in the whole energy interval (8.2–11.44 GeV) to have a deviation of at least this size, then the significance reduces to 1.4σ . Another feature that we observe is the enhancement of the differential cross section for the lowest energy region towards $|t|_{\text{max}}$ (Fig. 13), which can be interpreted as an s - or u -channel contribution. We estimate a 2.3σ significance of such a deviation when compared to a dipole fit of the differential cross section. All the above significance estimates include both statistical and systematic errors. The relevance of these features to the reaction mechanism will be discussed below.

Recently the J/ψ -007 experiment located in Hall C at Jefferson Lab published results on J/ψ photoproduction [41]. They reported $d\sigma/dt$ in 10 fine energy bins with similar total

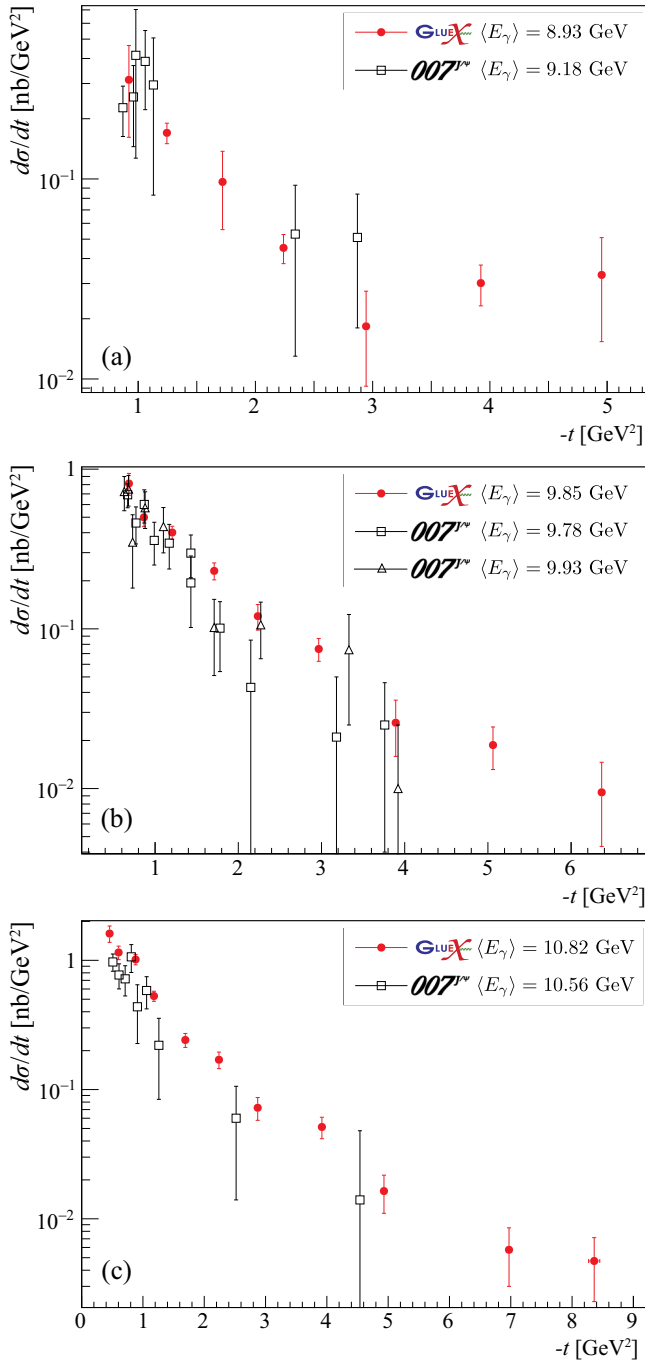


FIG. 14. Comparison of the differential cross sections for the three energy regions from this work to the measurements of the J/ψ -007 experiment closest in energy [41].

statistics as the results reported in this paper, though in a more narrow kinematic region both in energy and t . In Fig. 14 we compare the GlueX results for the three energy regions with the closest in energy differential cross sections of Ref. [41]. We see good agreement between the two experiments. When comparing the two results, recall the 20% scale uncertainty in the GlueX results and note the differences in the average energies.

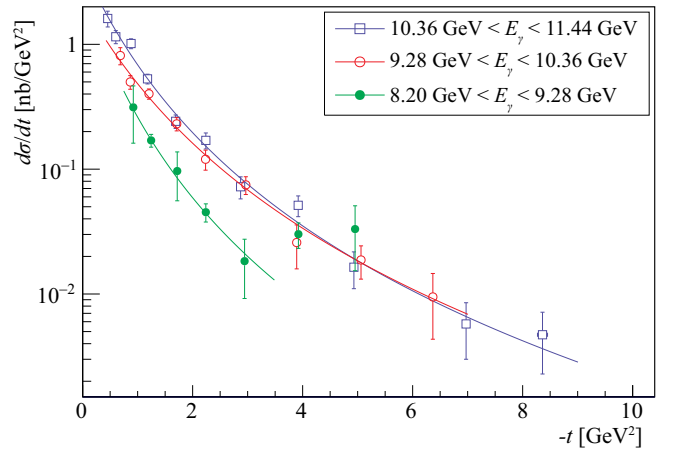


FIG. 15. The differential cross sections for the three energy regions fitted with $[d\sigma/dt(0)]/(1-t/m_s^2)^4$, where the cross section at $t=0$, $d\sigma/dt(0)$, and the mass scale, m_s , are free parameters.

The proximity of the GlueX data to the J/ψ threshold allows us to extrapolate the differential cross sections both in beam energy and t outside of the physical region and estimate the forward cross section at threshold, $d\sigma/dt(0)|_{\text{thr}}$. The forward cross section close to threshold, $d\sigma/dt(t=0, E_\gamma)$, enters in many theoretical models and plays an important role in understanding the J/ψ photoproduction and the J/ψ -proton (J/ψ -p) interaction [3,6,7,42]. The t dependence of the differential cross section can be related to the gluonic form factor $F(t)$ of the proton, which is usually parametrized with a dipole function, $\propto 1/(1-t/m_s^2)^2$ [2,16,43,44]. In Fig. 15 we show the results of fits to the measured differential cross sections with squared dipole functions of the form $[d\sigma/dt(0)]/(1-t/m_s^2)^4$, excluding the high- t region in the lowest energy region. The results of the fits are summarized in Table II.

The t slope is defined by the mass scale parameter, m_s , and the fit results for m_s are generally in good agreement with the lattice calculations [44] of the $A_g(t)$ gluon form factor that find $m_s = 1.13 \pm 0.06$ GeV. More precisely, such agreement of the J/ψ -007 data (also in agreement with our data, Fig. 14) with the lattice calculations was demonstrated in Ref. [41] using the holographic model of Ref. [13].

TABLE II. The forward differential cross sections, $d\sigma/dt(0)$, and the mass scale parameter, m_s , from the fits shown in Fig. 15 for the three average beam energies, $\langle E_\gamma \rangle$. The average momentum of the final state particles in the overall center-of-mass frame, q , for each beam energy bin is also given. Note, there is an overall 19.5% scale uncertainty of the results for $d\sigma/dt(0)$.

$\langle E_\gamma \rangle$ [GeV]	8.93	9.86	10.82
q [GeV]	0.499	0.767	0.978
$d\sigma/dt(0)$ [nb/GeV 2]	2.863	2.205	4.268
	± 1.95	± 0.380	± 0.564
m_s [GeV]	1.105	1.472	1.313
	± 0.168	± 0.075	± 0.049

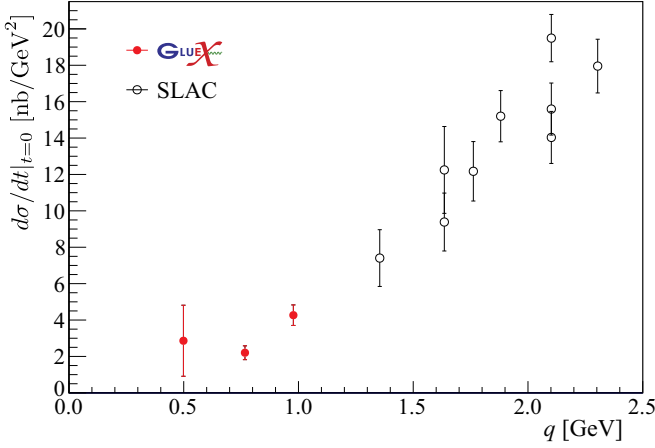


FIG. 16. The forward ($t = 0$) differential cross section as a function of final particle center-of-mass momentum from this work (filled red points) and SLAC [45] measurements (open black points).

The fits in Fig. 15 also directly give an extrapolation of the cross sections to $t = 0$, $d\sigma/dt(0)$, Table II. These results are plotted in Fig. 16 as a function of the final proton (or J/ψ) c.m. momentum, q , together with the SLAC measurements of $d\sigma/dt$ at $t = t_{\min}$ also extrapolated to $t = 0$ using their measured exponential slope of 2.9 GeV^{-2} [45]. Such a plot allows extrapolation of $d\sigma/dt(0)$ to the threshold, $d\sigma/dt(0)|_{\text{thr.}}$, that corresponds to $q = 0$. Reference [42] uses the VMD model and dispersion relations to parametrize the forward J/ψ - p scattering amplitude, $T^{\psi p}$, and to fit all existing J/ψ photoproduction data including those data taken at large center-of-mass energies. The parametrization is then used to fit the forward differential cross sections and estimate $d\sigma/dt(0)|_{\text{thr.}}$ —see Fig. 3 in Ref. [42], which is an analog to our Fig. 16. Alternatively, the extrapolation to threshold can be done by expanding $T^{\psi p}$ in partial waves, with the S wave being dominant near threshold. Initial extrapolations were previously reported along with the preliminary GlueX results [46], but will not be discussed further in this paper. It is of importance that the GlueX measurements are much closer to the threshold than the SLAC measurements [45] (the latter used in Ref. [42]), at the same time constraining $d\sigma/dt(0)|_{\text{thr.}}$ to lower values than the SLAC results and Ref. [42]. For the purpose of providing a quantitative estimate, let us assume $d\sigma/dt(0)|_{\text{thr.}}$ is close in value and uncertainty to the lowest- q data point in Fig. 16, $2.86 \pm 2.03 \text{ nb/GeV}^2$, where we have included the overall scale uncertainty. This value corresponds to a very small J/ψ - p scattering length, $\alpha_{J/\psi p}$, which is given by [7]

$$|\alpha_{J/\psi p}| = \sqrt{\frac{d\sigma}{dt}(0)|_{\text{thr.}} \frac{\gamma_\psi^2 k_{\gamma p}^2}{\alpha\pi \pi}}, \quad (6)$$

where $k_{\gamma p}$ is the c.m. momenta of the initial particles and γ_ψ is the photon- J/ψ coupling constant obtained from the $J/\psi \rightarrow e^+e^-$ decay width. We find $|\alpha_{J/\psi p}| = (21.3 \pm 8.2) \times 10^{-3} \text{ fm}$, which, compared to the size of the proton of $\sim 1 \text{ fm}$ scale, indicates a very weak J/ψ - p interaction. However, note that the VMD model is used in Eq. (6) to extract this value.

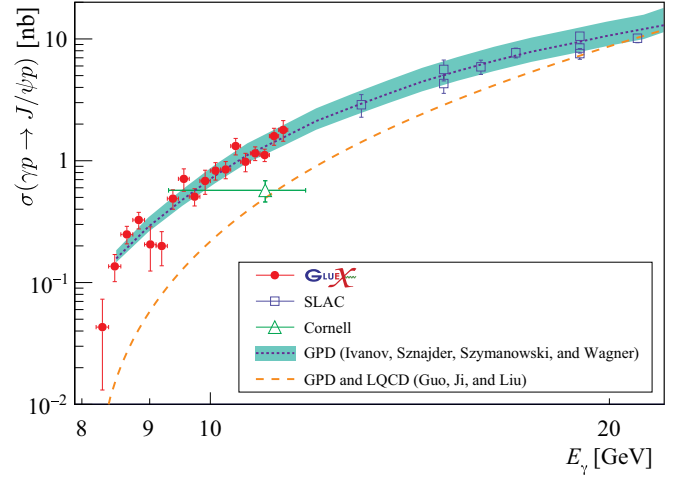


FIG. 17. Comparison of the J/ψ total cross sections from this work (GlueX) to the SLAC [45] and Cornell [47] data and two QCD theoretical calculations in the two-gluon exchange factorization model (in LO) from Ref. [48] and from Ref. [10]. The latter calculation uses gravitational form factors from lattice calculations [44]. The SLAC total cross sections are estimated from their $d\sigma/dt|_{t=t_{\min}}$ measurements [45] assuming a dipole t dependence from the fit of our differential cross section at the highest energy, Fig. 15. The error bars shown for the GlueX data are the statistical and systematic errors summed in quadrature.

We can use the mass scale m_s from the fits in Fig. 15 (Table II) to estimate the proton mass radius as prescribed in Ref. [11],

$$\sqrt{\langle r_m^2 \rangle} = \sqrt{\frac{6}{m_p} \frac{dG(t)}{dt} \Big|_{t=0}} = \sqrt{\frac{12}{m_s^2}}, \quad (7)$$

where the scalar gravitational form factor, $G(t)$, is related to the measured t distributions through the VMD model. Equation (7) gives $\sqrt{\langle r_m^2 \rangle} = 0.619 \pm 0.094 \text{ fm}$, $0.464 \pm 0.024 \text{ fm}$, and $0.521 \pm 0.020 \text{ fm}$ for $E_\gamma = 8.93, 9.86, \text{ and } 10.82 \text{ GeV}$, respectively. More sophisticated estimations of the proton mass radius require knowledge of the $A(t)$ and $C(t)$ gravitational form factors separately [10,41].

In Fig. 17 we compare our total cross section results to models that assume factorization of the J/ψ photoproduction into a hard quark-gluon interaction and the GPDs describing the partonic distributions of the proton. This factorization in exclusive heavy-meson photoproduction in terms of GPDs was studied in the kinematic region of low $|t|$ and high beam energies [8]. The factorization was explicitly demonstrated by direct leading order (LO) and next-to-leading order (NLO) calculations. In Ref. [10], it was shown that in the limit of high meson masses and at LO, the factorization in terms of gluon GPDs is still valid down to the threshold. Calculations in this framework were performed for the J/ψ photoproduction cross section using parametrizations of the gravitational form factors obtained from the lattice results of Ref. [44]. These calculations for the total cross section are compared to our measurements in Fig. 17. While they agree better with the SLAC data at higher energies, they underestimate our near-

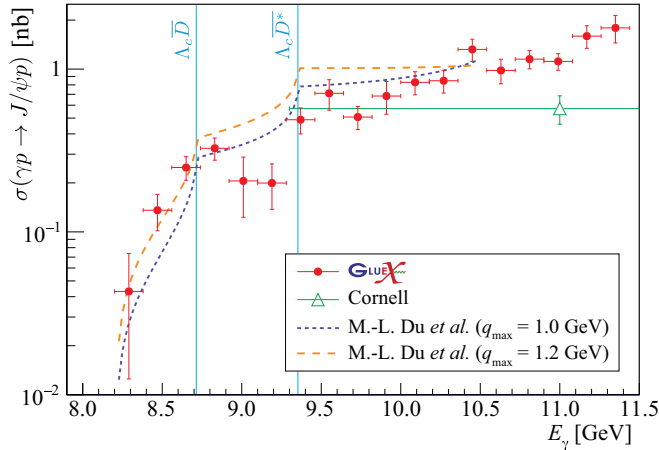


FIG. 18. Comparison of the GlueX J/ψ total cross section to open charm calculations [19]. The thresholds of $\Lambda_c \bar{D}$ (8.71 GeV) and $\Lambda_c \bar{D}^*$ (9.35 GeV) are shown as vertical lines. The error bars shown for the GlueX data are the statistical and systematic errors summed in quadrature.

threshold measurements. Recently, the authors of Ref. [8] extended their calculations to the threshold region at LO [48]. These calculations, plotted also in Fig. 17, are in a very good agreement with the total cross section measurements. Attempts to include the NLO contribution result in large uncertainties due to the poor knowledge of the corresponding GPD functions in this kinematic region [49]. This indicates that our measurements can strongly constrain the relevant gluon GPD functions.

The authors of Ref. [19] propose an alternative mechanism of J/ψ photoproduction with a dominant exchange of open-charm channels $\Lambda_c \bar{D}$ and $\Lambda_c \bar{D}^*$ in box diagrams. We show the total cross section results of this model in Fig. 18, and find good qualitative agreement with our measurements. In particular, in the data we see structures peaking at both the $\Lambda_c \bar{D}$ and $\Lambda_c \bar{D}^*$ thresholds that can be interpreted as the cusps expected with this reaction mechanism. However, the exchange of heavy hadrons in this model implies a very shallow t dependence in the differential cross sections. This is not supported by the steeply falling cross sections we observe, as shown in Fig. 15. Therefore, our differential cross section measurements do not support a dominant contribution from these open charm exchanges, although the enhancement at high t observed for the lowest beam energy region is consistent with a possible contribution from these exchanges. Alternatively, in Ref. [50] it was shown that the high- t enhancement can be explained by u -channel contribution assuming factorization in terms of Transition Distribution Amplitudes [51].

In Ref. [52], the model-independent effective range expansion was used to parametrize the lowest partial waves. Fits to the total and differential cross sections from this paper and from Ref. [41] show that the expansion is rapidly convergent, with the $L \leq 3$ waves saturating the forward peak in the measured photon energy range. Furthermore, the energy dependence of the total cross section near the open-charm

thresholds was shown to be consistent with the appearance of $\Lambda_c \bar{D}^{(*)}$ intermediate states, as suggested by Ref. [19].

It is important to be able to understand the dynamics underlying J/ψ photoproduction at threshold, and possibly to identify a kinematic region that can be used to extract the proton gluonic form factors. Based on the t -slopes of the differential cross sections (Fig. 15) and also the results of Ref. [41], the differential cross section at low t values is consistent with being dominantly due to gluonic exchange. However, the possible structures in the total cross section energy dependence and the flattening of the differential cross section near threshold are consistent with contributions from open-charm intermediate states. So far, from the analyses of Ref. [52] it is not possible to distinguish between the gluon and open-charm exchange mechanisms. Certainly, further theoretical work is needed to understand the mechanism of near-threshold J/ψ production and its relation to the gluonic structure of the proton, especially since hints of open charm production are visible. On the experimental side, higher statistics are needed to confirm the structures in the total cross section and the enhancement in the t dependence, the statistical significance of which at present does not allow making of definitive conclusions.

ACKNOWLEDGMENTS

We thank A. N. H. Blin, A. Pilloni, A. P. Szczepaniak, and D. Winney for the fruitful discussions of the interpretation of the results. We acknowledge the outstanding efforts of the staff of the Accelerator and the Physics Divisions at Jefferson Lab that made the experiment possible. This work was supported in part by the U.S. Department of Energy, the U.S. National Science Foundation, the German Research Foundation, Forschungszentrum Jülich GmbH, GSI Helmholtzzentrum für Schwerionenforschung GmbH, the Natural Sciences and Engineering Research Council of Canada, the Russian Foundation for Basic Research, the UK Science and Technology Facilities Council, the Chilean Comisión Nacional de Investigación Científica y Tecnológica, the National Natural Science Foundation of China, and the China Scholarship Council. This material is based upon work supported by the U.S. Department of Energy, Office of Science, Office of Nuclear Physics under Contract No. DE-AC0506OR23177. This research used resources of the National Energy Research Scientific Computing Center (NERSC), a U.S. Department of Energy Office of Science User Facility operated under Contract No. DE-AC02-05CH11231. This work used the Extreme Science and Engineering Discovery Environment (XSEDE), which is supported by National Science Foundation Grant No. ACI-1548562. Specifically, it used the Bridges system, which is supported by National Science Foundation Award No. ACI-1445606, at the Pittsburgh Supercomputing Center (PSC).

APPENDIX: NUMERICAL RESULTS

The numerical results for the total and differential cross sections are given in Tables III–VI.

TABLE III. $\gamma p \rightarrow J/\psi p$ total cross sections in bins of beam energy. The first uncertainties are statistical, and the second are systematic.

Energy bin [GeV]	σ [nb]
8.20–8.38	$0.043 \pm 0.012 \pm 0.027$
8.38–8.56	$0.136 \pm 0.022 \pm 0.026$
8.56–8.74	$0.249 \pm 0.029 \pm 0.029$
8.74–8.92	$0.326 \pm 0.048 \pm 0.016$
8.92–9.10	$0.206 \pm 0.059 \pm 0.056$
9.10–9.28	$0.200 \pm 0.060 \pm 0.018$
9.28–9.46	$0.489 \pm 0.087 \pm 0.019$
9.46–9.64	$0.710 \pm 0.134 \pm 0.064$
9.64–9.82	$0.507 \pm 0.080 \pm 0.019$
9.82–10.00	$0.683 \pm 0.100 \pm 0.116$
10.00–10.18	$0.829 \pm 0.119 \pm 0.064$
10.18–10.36	$0.848 \pm 0.123 \pm 0.059$
10.36–10.54	$1.321 \pm 0.193 \pm 0.067$
10.54–10.72	$0.981 \pm 0.134 \pm 0.104$
10.72–10.90	$1.151 \pm 0.140 \pm 0.051$
10.90–11.08	$1.114 \pm 0.126 \pm 0.034$
11.08–11.26	$1.594 \pm 0.208 \pm 0.144$
11.26–11.44	$1.791 \pm 0.344 \pm 0.026$

TABLE IV. $\gamma p \rightarrow J/\psi p$ differential cross sections in the 8.2–9.28 GeV beam energy range, average t and beam energy in bins of t . The first cross section uncertainties are statistical, and the second are systematic. The overall average beam energy is 8.93 GeV.

t bin [GeV ²]	$\langle t \rangle$ [GeV ²]	$\langle E_\gamma \rangle$ [GeV]	$d\sigma/dt$ [nb/GeV ²]
0.77–1.00	0.92	9.14	$0.313 \pm 0.092 \pm 0.120$
1.00–1.50	1.25	8.96	$0.170 \pm 0.018 \pm 0.008$
1.50–2.00	1.72	8.80	$0.097 \pm 0.010 \pm 0.040$
2.00–2.50	2.24	8.77	$0.045 \pm 0.007 \pm 0.003$
2.50–3.50	2.94	8.78	$0.018 \pm 0.003 \pm 0.009$
3.50–4.50	3.92	8.95	$0.030 \pm 0.006 \pm 0.004$
4.50–5.75	4.95	9.10	$0.033 \pm 0.013 \pm 0.012$

TABLE V. $\gamma p \rightarrow J/\psi p$ differential cross sections in the 9.28–10.36 GeV beam energy range, average t and beam energy in bins of t . The first cross section uncertainties are statistical, and the second are systematic. The overall average beam energy is 9.86 GeV.

t bin [GeV ²]	$\langle t \rangle$ [GeV ²]	$\langle E_\gamma \rangle$ [GeV]	$d\sigma/dt$ [nb/GeV ²]
0.49–0.77	0.69	10.00	$0.813 \pm 0.088 \pm 0.092$
0.77–1.00	0.87	9.85	$0.499 \pm 0.061 \pm 0.016$
1.00–1.50	1.21	9.83	$0.401 \pm 0.037 \pm 0.010$
1.50–2.00	1.71	9.83	$0.231 \pm 0.027 \pm 0.006$
2.00–2.50	2.24	9.82	$0.120 \pm 0.021 \pm 0.007$
2.50–3.50	2.97	9.84	$0.075 \pm 0.011 \pm 0.005$
3.50–4.50	3.89	9.86	$0.026 \pm 0.008 \pm 0.006$
4.50–5.75	5.06	9.76	$0.019 \pm 0.005 \pm 0.002$
5.75–8.10	6.37	9.93	$0.009 \pm 0.004 \pm 0.003$

TABLE VI. $\gamma p \rightarrow J/\psi p$ differential cross sections in the 10.36–11.44 GeV beam energy range, average t and energy, in bins of t . The first cross section uncertainties are statistical, and the second are systematic. The overall average beam energy is 10.82 GeV.

t bin [GeV ²]	$\langle t \rangle$ [GeV ²]	$\langle E_\gamma \rangle$ [GeV]	$d\sigma/dt$ [nb/GeV ²]
0.35–0.49	0.46	10.96	$1.611 \pm 0.187 \pm 0.139$
0.49–0.77	0.60	10.87	$1.150 \pm 0.084 \pm 0.109$
0.77–1.00	0.88	10.85	$1.015 \pm 0.089 \pm 0.023$
1.00–1.50	1.18	10.86	$0.529 \pm 0.042 \pm 0.023$
1.50–2.00	1.69	10.86	$0.242 \pm 0.029 \pm 0.008$
2.00–2.50	2.24	10.83	$0.170 \pm 0.025 \pm 0.003$
2.50–3.50	2.87	10.82	$0.072 \pm 0.012 \pm 0.008$
3.50–4.50	3.92	10.81	$0.051 \pm 0.009 \pm 0.002$
4.50–5.75	4.93	10.78	$0.016 \pm 0.005 \pm 0.001$
5.75–8.10	6.97	10.70	$0.0058 \pm 0.0026 \pm 0.0008$
8.10–10.30	8.36	10.70	$0.0047 \pm 0.0024 \pm 0.0002$

- [1] A. Ali *et al.* (GlueX collaboration), *Phys. Rev. Lett.* **123**, 072001 (2019).
- [2] L. Frankfurt and M. Strikman, *Phys. Rev. D* **66**, 031502(R) (2002).
- [3] D. Kharzeev, H. Satz, A. Syamtomov, and G. Zinovev, *Nucl. Phys. A* **661**, 568 (1999).
- [4] Y. Hatta and D.-L. Yang, *Phys. Rev. D* **98**, 074003 (2018).
- [5] W. Kou, R. Wang, and X. Chen, [arXiv:2104.12962](https://arxiv.org/abs/2104.12962).
- [6] I. I. Strakovsky, D. Epifanov, and L. Pentchev, *Phys. Rev. C* **101**, 042201(R) (2020).
- [7] L. Pentchev and I. I. Strakovsky, *Eur. Phys. J. A* **57**, 56 (2021).
- [8] D. Y. Ivanov, A. Schafer, L. Szymanowski, and G. Krasnikov, *Eur. Phys. J. C* **34**, 297 (2004).
- [9] Y. Hatta and M. Strikman, *Phys. Lett. B* **817**, 136295 (2021).
- [10] Y. Guo, X. Ji, and Y. Liu, *Phys. Rev. D* **103**, 096010 (2021).
- [11] D. E. Kharzeev, *Phys. Rev. D* **104**, 054015 (2021).
- [12] X. Ji, Y. Liu, and I. Zahed, *Phys. Rev. D* **103**, 074002 (2021).
- [13] K. A. Mamo and I. Zahed, *Phys. Rev. D* **103**, 094010 (2021).
- [14] R. Wang, W. Kou, Y.-P. Xie, and X. Chen, *Phys. Rev. D* **103**, L091501 (2021).
- [15] Y. Hatta, A. Rajan, and D.-L. Yang, *Phys. Rev. D* **100**, 014032 (2019).
- [16] K. A. Mamo and I. Zahed, *Phys. Rev. D* **101**, 086003 (2020).
- [17] K. A. Mamo and I. Zahed, *Phys. Rev. D* **104**, 066023 (2021).
- [18] P. Sun, X.-B. Tong, and F. Yuan, *Phys. Rev. D* **105**, 054032 (2022).
- [19] M.-L. Du, V. Baru, F.-K. Guo, C. Hanhart, U.-G. Meißner, A. Nefediev, and I. Strakovsky, *Eur. Phys. J. C* **80**, 1053 (2020).
- [20] R. Aaij *et al.* (LHCb Collaboration), *Phys. Rev. Lett.* **115**, 072001 (2015).

- [21] R. Aaij *et al.* (LHCb Collaboration), *Phys. Rev. Lett.* **122**, 222001 (2019).
- [22] Q. Wang, X.-H. Liu, and Q. Zhao, *Phys. Rev. D* **92**, 034022 (2015).
- [23] V. Kubarovsky and M. B. Voloshin, *Phys. Rev. D* **92**, 031502(R) (2015).
- [24] M. Karliner and J. Rosner, *Phys. Lett. B* **752**, 329 (2016).
- [25] A. N. Hiller Blin, C. Fernandez-Ramirez, A. Jackura, V. Mathieu, V. I. Mokeev, A. Pilloni, and A. P. Szczepaniak, *Phys. Rev. D* **94**, 034002 (2016).
- [26] S. Adhikari, C. Akondi, H. Al Ghoul, A. Ali, M. Amaryan, E. Anassontzis, A. Austregesilo, F. Barbosa, J. Barlow, A. Barnes *et al.*, *Nucl. Instrum. Methods Phys. Res., Sect. A* **987**, 164807 (2021).
- [27] F. Barbosa, C. Hutton, A. Sitnikov, A. Somov, S. Somov, and I. Tolstukhin, *Nucl. Instrum. Methods Phys. Res., Sect. A* **795**, 376 (2015).
- [28] E. Pooser, F. Barbosa, W. Boeglin, C. Hutton, M. Ito, M. Kamel, P. K. A. LLodra, N. Sandoval, S. Taylor, T. Whitlatch, S. Worthington, C. Yero, and B. Zihlmann, *Nucl. Instrum. Methods Phys. Res., Sect. A* **927**, 330 (2019).
- [29] N. Jarvis, C. Meyer, B. Zihlmann, M. Staib, A. Austregesilo, F. Barbosa, C. Dickover, V. Razmyslovich, S. Taylor, Y. Van Haarlem *et al.*, *Nucl. Instrum. Methods Phys. Res., Sect. A* **962**, 163727 (2020).
- [30] L. Pentchev, F. Barbosa, V. Berdnikov, D. Butler, S. Furletov, L. Robison, and B. Zihlmann, *Nucl. Instrum. Methods Phys. Res., Sect. A* **845**, 281 (2017).
- [31] T. D. Beattie, A. M. Foda, C. L. Henschel, S. Katsaganis, S. T. Krueger, G. J. Lolos, Z. Papandreou *et al.*, *Nucl. Instrum. Methods Phys. Res., Sect. A* **896**, 24 (2018).
- [32] R. Paremuzyan (private communication, 2017).
- [33] E. Berger, M. Diehl, and B. Pire, *Eur. Phys. J. C* **23**, 675 (2002).
- [34] K. Borah, R. J. Hill, G. Lee, and O. Tomalak, *Phys. Rev. D* **102**, 074012 (2020).
- [35] J. Allison *et al.*, *Nucl. Instrum. Methods Phys. Res., Sect. A* **835**, 186 (2016).
- [36] W. Verkerke and D. Kirkby, https://root.cern/download/doc/RooFit_Users_Manual_2.91-33.pdf.
- [37] M. Tanabashi *et al.* (Particle Data Group), *Phys. Rev. D* **98**, 030001 (2018).
- [38] M. Heller, O. Tomalak, and M. Vanderhaeghen, *Phys. Rev. D* **97**, 076012 (2018).
- [39] M. Boer, Jefferson Lab, Hall C public document #1000, <https://hallweb.jlab.org/docpublic/ShowDocument?docid=1000> (2019).
- [40] M. Boër, M. Guidal, and M. Vanderhaeghen, *Eur. Phys. J. A* **51**, 103 (2015).
- [41] B. Duran, Z.-E. Meziani, S. Joosten, M. K. Jones, S. Prasad, C. Peng, W. Armstrong, H. Atac, E. Chudakov, H. Bhatt, D. Bhetuwal, M. Boer, A. Camsonne, J.-P. Chen, M. M. Dalton, N. Deokar, M. Diefenthaler, J. Dunne, L. El Fassi, E. Fuchey *et al.*, *Nature (London)* **615**, 813 (2023).
- [42] O. Gryniuk and M. Vanderhaeghen, *Phys. Rev. D* **94**, 074001 (2016).
- [43] X.-B. Tong, J.-P. Ma, and F. Yuan, *Phys. Lett. B* **823**, 136751 (2021).
- [44] P. E. Shanahan and W. Detmold, *Phys. Rev. D* **99**, 014511 (2019).
- [45] U. Camerini, J. Learned, R. Prepost, C. Spencer, D. Wisner, W. Ash, R. L. Anderson, D. M. Ritson, D. Sherden, and C. K. Sinclair, *Phys. Rev. Lett.* **35**, 483 (1975).
- [46] L. Pentchev, https://indico.jlab.org/event/344/contributions/10353/attachments/8401/12067/LPentchev_Jpsi_QNP2022.pdf.
- [47] B. Gittelmann, K. M. Hanson, D. Larson, E. Loh, A. Silverman, and G. Theodosiou, *Phys. Rev. Lett.* **35**, 1616 (1975).
- [48] D. Ivanov, P. Sznajder, L. Szymanowski, and J. Wagner (private communication, 2022).
- [49] P. Sznajder and J. Wagner (private communication, 2022).
- [50] B. Pire, K. M. Semenov-Tian-Shansky, A. A. Shaikhutdinova, and L. Szymanowski, [arXiv:2212.07688](https://arxiv.org/abs/2212.07688) (2022).
- [51] B. Pire, K. Semenov-Tian-Shansky, and L. Szymanowski, *Phys. Rep.* **940**, 1 (2021).
- [52] D. Winney, C. Fernandez-Ramirez, A. Pilloni, A. N. H. Blin, M. Albaladejo, L. Bibrzycki, N. Hammoud, J. Liao, V. Mathieu, G. Montana, R. J. Perry, V. Shastri, W. A. Smith, and A. P. Szczepaniak, [arXiv:2305.01449](https://arxiv.org/abs/2305.01449).